Available online at www.sciencedirect.com
ScienceDirect
International Journal of Heat and Mass Transfer 50 (2007) 1255–1262
International Journal of HEAT and MASS TRANSFER
www.elsevier.com/locate/ijhmt

Prediction of the maximum heat transfer capability of two-phase heat spreaders – Experimental validation

Romuald Rullière, Frédéric Lefèvre *, Monique Lallemand

CETHIL, UMR 5008 CNRS-INSA-UCB, INSA, 20 av. A. Einstein, 69621 Villeurbanne Cedex, France

Received 10 April 2006; received in revised form 18 September 2006
Available online 22 November 2006

Abstract

The present paper is devoted to an experimental study to determine the thermal behaviour of a two-phase heat spreader (TPHS) with micro-grooves. The proposed application is the cooling of fuel cell systems. This TPHS aims at reducing the volume of actual cooling systems and to homogenize the temperature in the hearth of fuel cells. The TPHS is flat with a wide evaporating area (190×90 mm^2) compared to the condenser area (30×90 mm^2). It has been tested with three working fluids: water, methanol and *n*-pentane. Experimental results obtained with methanol show a temperature difference lower than 1.6 K on the entire evaporator area for a heat transfer rate equal to 85 W and a working temperature equal to 70 °C. The TPHS has been tested in both horizontal and vertical favourable orientation (thermosyphon orientation). The temperature field is similar in both cases for heat transfer rates lower than 155 W. In horizontal orientation, a confocal microscope is used to measure the meniscus curvature radius along the grooves. A two-phase flow model allowing the calculation of the meniscus radius, the liquid and vapour pressures and the liquid and vapour velocities along the TPHS is developed. The comparison between experimental and model results shows the good ability of the numerical model to predict the meniscus curvature radii from which the maximum heat transfer capability of the TPHS is depending.

Keywords: Two-phase heat spreader; Meniscus curvature; Heat transfer capability; Micro-grooves

1. Introduction

The development of fuel cells for electric power production in static or on-board systems needs thermal control. Proton exchange membrane fuel cells (PEMFC) have working temperatures varying from 60 °C to 100 °C. Their efficiency can reach about 50%, which involves outward heat dissipation. The heat production has to be removed from important areas inside the fuel cells (200–1000 cm^2) with heat fluxes reaching about 0.5 W cm^{-2}. At the moment, forced convection water flow is generally used as the cooling system, which permits to remove the heat production. Nevertheless, it does not homogenize efficiently the temperature inside a PEMFC, which is required to obtain high efficiencies. A two-phase cooling device can be used to homogenize the temperature and to reduce the global volume of the cooling system inside a PEMFC. Among these devices, two-phase heat spreaders (TPHSs) that are often present in electronic cooling [1,2] can be used to reach this purpose.

TPHS are very efficient cooling systems that are able to transfer high heat fluxes with small temperature gradients. They are used for their heat transfer capacity as well as their heat spreading characteristics. A TPHS is a cavity of small thickness filled with a two-phase working fluid. Heat sources and heat sinks are located anywhere on the cavity with the other parts being insulated [2]. Vapour is generated at the heat source level (evaporator) and it condenses at the heat sink level (condenser). The liquid returns from the evaporator to the condenser through a capillary structure made of micro-grooves, meshes or sintered powder wicks.

Unlike classical arrays of micro heat pipes (MHPs) that are made of several single tubes working independently

* Corresponding author. Tel.: +33 4 7243 8251; fax: +33 4 7243 8811.
E-mail address: frederic.lefevre@insa-lyon.fr (F. Lefèvre).

0017-9310/$ - see front matter © 2006 Elsevier Ltd. All rights reserved.
doi:10.1016/j.ijheatmasstransfer.2006.09.015

Nomenclature

A	cross-section area, m^2
c	aspect ratio
f	friction coefficient
g	gravitational acceleration, $m\ s^{-2}$
h	heat transfer coefficient, $W\ m^{-2}\ K^{-1}$
h_{lv}	latent heat of vaporization, $J\ kg^{-1}$
l	width, m
L	length, m
P	pressure, Pa
Po	Poiseuille number
q	heat flux, $W\ m^{-2}$
r	meniscus curvature radius, m
Re	Reynolds number
T	temperature, K
u, v	velocities, $m\ s^{-1}$
x, y, z	coordinates, m

Greek symbols

λ	thermal conductivity, $W\ m^{-1}\ K^{-1}$
μ	dynamic viscosity, Pa s
ρ	density, $kg\ m^{-3}$
θ	contact angle, rad
σ	surface tension, $N\ m^{-1}$
τ	shear stress, $N\ m^{-2}$

Subscripts

cal	calculated
cond	condensation
g	groove
int	interfacial
l	liquid
max	maximum
min	minimum
sat	saturation
v	vapour
w	wall

[3–7], TPHSs have a single vapour core in which a capillary structure is inserted. Compared with MHP arrays of same thickness, the vapour hydraulic diameter of TPHSs is higher, which reduces the vapour pressure drop and the shear stress at the liquid–vapour interface due to counter-current flows. As a result, TPHSs have better heat transfer capabilities. TPHSs are usually made of copper, aluminium or silicon. Their capillary structure can be either 1D or 2D for the liquid flow. One-dimensional capillary structures are made of micro-grooves machined in the channel wall [8–12]. Two-dimensional capillary structures are made of meshes [13], crossed grooves [14–16], radial grooves [17,18] or sintered powder wicks [19]. Some authors [17,18,20] have obtained better performances by protecting the liquid flow from the vapour flow by a separation plate located in the adiabatic area.

In this paper, an experimental study is presented to show the thermal behaviour of a two-phase heat spreader with a high evaporating area compared to the condenser area. A confocal microscope is used to measure the meniscus curvature radius along a groove in working configuration. The measurements are compared to the results of a two-phase flow model, based on the balance equations and the Young–Laplace equation. This model allows the calculation of the maximum heat transfer capability of a TPHS that depends on both the geometrical characteristics and the working fluid properties.

2. Experimental set-up

For the proposed application of PEMFC cooling, a 1D capillary structure made of micro-grooves has been used to drain the liquid from the condenser to the evaporator. Unlike classical TPHS applications, in which the heat source is small compared to the adiabatic and the heat sink regions, PEMFC cooling involves a big heat source, a small heat sink and a small adiabatic region.

The TPHS under investigation is shown in Fig. 1. Its capillary structure, of dimensions $230 \times 90\ mm^2$, is made of 109 longitudinal micro-grooves, machined in a copper plate. Each groove has a rectangular cross-section of height and width equals to 380 μm and 400 μm, respectively. The distance between two grooves is equal to 400 μm. The vapour space height is equal to 1.6 mm and the wall thickness under the grooves is equal to 2 mm. The TPHS is hermetically sealed on its upper face with a borosilicate glass

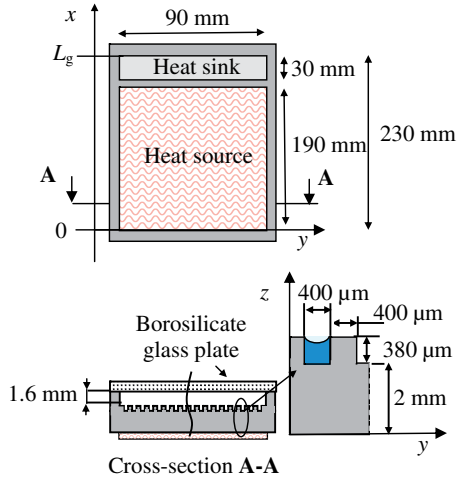

Fig. 1. Schematic of the copper TPHS.

plate, which allows the liquid/vapour meniscus observation in the grooves. The heat source is located on the copper wall (Fig. 2). It is a thick resistor film of dimensions 190×90 mm^2, which allows the simulation of heat dissipation inside a PEMFC. This resistor of 2.1 Ω is supplied by a 0–36 V DC power supply. The heat sink is a water heat exchanger of dimensions 30×90 mm^2. The water flow rate is constant and the inlet temperature is regulated by means of a thermostatic bath in order to have a constant working temperature when the heat transfer rate increases. The heat source and the heat sink are separated by an adiabatic area of length equal to 10 mm. Unlike classical TPHS applications, the adiabatic area is very small leading to important temperature gradients in it. The working temperature of the TPHS is measured by a thermocouple located in the middle of the borosilicate glass plate, which is thermally insulated like the entire TPHS during the thermal tests. Two series of seven thermistors are located symmetrically along the TPHS wall and the value of their resistance is recorded by a Keithley 2700 multimeter.

A confocal microscope is used to measure the location of the meniscus curvature radius in the grooves, the TPHS being in horizontal orientation (Fig. 3). The optical sensor has a vertical measuring range along the z axis of 350 μm and its accuracy is lower than 1 μm in the y and z directions. Once the top of the groove is located by the sensor, measurements are realised along the y axis with a step

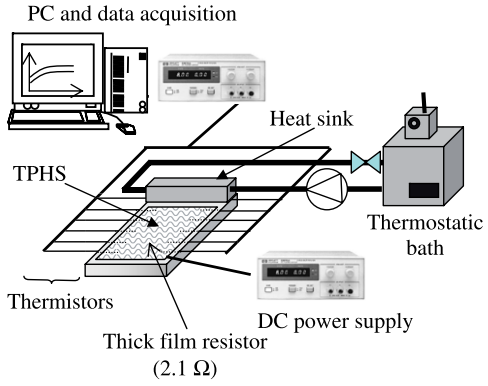

Fig. 2. Schematic of the TPHS test apparatus.

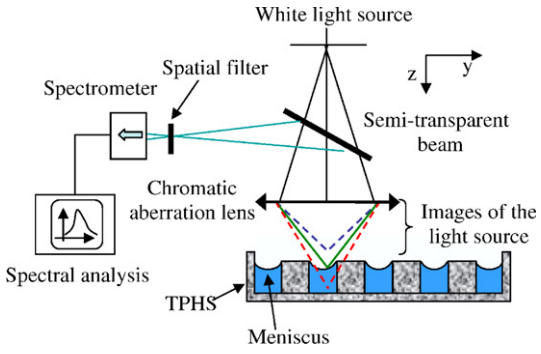

Fig. 3. Meniscus measurement by confocal microscopy.

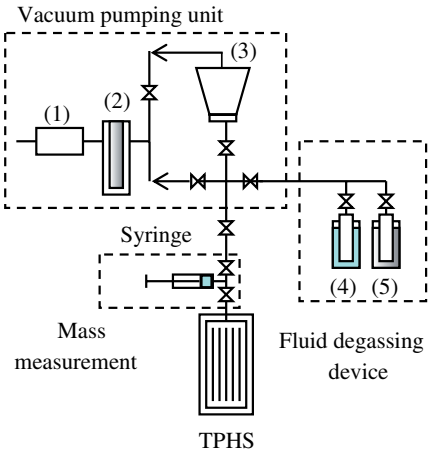

Fig. 4. Schematic of the experimental set-up for TPHS degassing, filling and for fill charge measurement; (1) vane rotary type pump, (2) liquid nitrogen trap, (3) turbomolecular pump, (4) heated vessel, (5) liquid nitrogen cooled vessel.

equal to 5 μm. The coordinates y and z of the meniscus are recorded. The resulting data are used to estimate through a least square method the radius and the centre coordinates of a circle that fit at best the experimental data. The part of the optical sensor light that is not reflected generates heat inside the device, but the optical sensor velocity along the y axis is fast enough (about 1 mm s^{-1}) for not thermally disturbing the measurement. Several similar measurements are realised along the x axis to obtain the meniscus curvature radius variation from the evaporator to the condenser.

Before the thermal tests, the TPHS has to be degassed and filled. In order to promote surface wetting, the TPHS is first cleaned [21]. The TPHS and the working fluid are degassed carefully to eliminate the amount of non-condensable gases (Fig. 4). The method of evacuating the non-condensable gases from the working fluid is based on the fluid solidification under vacuum. The fluid contained in the heated vessel (4) vaporizes, releases non-condensable gases and solidifies in the vessel (5), dipped into liquid nitrogen. The non-condensable gases are evacuated by vacuum pumps (1, 3). The degassed working fluid, which is then vaporized in the heated vessel (5), is introduced as a vapour and then condenses in a syringe. The TPHS is degassed by heating during vacuum pumping at 10^{-6} mbar. A known volume of fluid contained in the syringe is then injected in the TPHS.

3. A one-dimensional two-phase flow model

A one-dimensional two-phase flow model has been developed for a two-phase heat spreader with longitudinal grooves in horizontal orientation. The TPHS is divided into several control volumes for which the balance equations are written for both the liquid and the vapour phases. For the liquid and vapour mass balance, we obtain respectively:

$$\frac{\mathrm{d}(A_\mathrm{l}u_\mathrm{l})}{\mathrm{d}x}\mathrm{d}x = L_\mathrm{int}v_\mathrm{int}\mathrm{d}x \tag{1}$$

$$\frac{\mathrm{d}(A_\mathrm{v}u_\mathrm{v})}{\mathrm{d}x}\mathrm{d}x = -\frac{\rho_\mathrm{l}}{\rho_\mathrm{v}}L_\mathrm{int}v_\mathrm{int}\mathrm{d}x \tag{2}$$

where subscripts l and v denote the liquid and the vapour, respectively. A is the cross-section, L_int is the liquid–vapour interfacial length, x is the axial coordinate, u is the velocity and ρ the density. The transversal velocity of condensation or evaporation v_int is calculated from the energy balance:

$$v_\mathrm{int} = -\frac{q}{\rho_\mathrm{l}h_\mathrm{lv}} \tag{3}$$

where h_lv is the latent heat of vaporization and q the heat flux at the liquid–vapour interfacial area, which is assumed to be uniform in the condenser and evaporator sections and equal to zero in the adiabatic section.

Two additional equations are obtained from the momentum balance equations:

$$\rho_\mathrm{l}\frac{\mathrm{d}(A_\mathrm{l}u_\mathrm{l}^2)}{\mathrm{d}x}\mathrm{d}x = -A_\mathrm{l}\frac{\mathrm{d}P_\mathrm{l}}{\mathrm{d}x}\mathrm{d}x + \frac{\mathrm{d}A_\mathrm{l}}{\mathrm{d}x}(P_\mathrm{v}-P_\mathrm{l})\mathrm{d}x + |\tau_\mathrm{lw}|L_\mathrm{lw}\mathrm{d}x + |\tau_\mathrm{int}|L_\mathrm{int}\mathrm{d}x \tag{4}$$

$$\rho_\mathrm{v}\frac{\mathrm{d}(A_\mathrm{v}u_\mathrm{v}^2)}{\mathrm{d}x}\mathrm{d}x = -A_\mathrm{v}\frac{\mathrm{d}P_\mathrm{v}}{\mathrm{d}x}\mathrm{d}x + \frac{\mathrm{d}A_\mathrm{v}}{\mathrm{d}x}(P_\mathrm{l}-P_\mathrm{v})\mathrm{d}x - |\tau_\mathrm{vw}|L_\mathrm{vw}\mathrm{d}x - |\tau_\mathrm{int}|L_\mathrm{int}\mathrm{d}x \tag{5}$$

where P is the pressure, τ_lw and τ_vw the liquid-wall and vapour-wall shear stresses and τ_int is the interfacial shear stress. L_vw and L_lw are the vapour-wall and liquid-wall wetted lengths, respectively.

The wall shear stress is calculated by assuming liquid and vapour laminar flows:

$$\tau = \frac{1}{2}\rho u^2 f \quad \text{with } f = \frac{Po}{Re} \tag{6}$$

where f is the friction coefficient, Po is the Poiseuille number and Re is the Reynolds number. For a rectangular groove, the Poiseuille number can be calculated using the Shah and London law [22] for the liquid and the vapour:

$$Po = 24\left(1 - 1.3553c_\mathrm{min} + 1.9467c_\mathrm{min}^2 - 1.7012c_\mathrm{min}^3 + 0.9564c_\mathrm{min}^4 - 0.2537c_\mathrm{min}^5\right) \tag{7}$$

where c_min is the minimum aspect ratio between the height and the width of the cross-section. The interfacial shear stress is a parameter that is difficult to estimate, especially in this configuration where phase change phenomena occur nearly all along the groove. As it will be seen in the next section, this parameter has a little influence on the results for this TPHS.

In Eqs. (1)–(5), A_l, A_v, L_vw, L_lw, and L_int depend on the groove geometry and on the meniscus radius r that is calculated by deriving the Laplace–Young equation with respect to x:

$$\frac{\mathrm{d}P_\mathrm{l}}{\mathrm{d}x} = \frac{\mathrm{d}P_\mathrm{v}}{\mathrm{d}x} - \frac{\mathrm{d}}{\mathrm{d}x}\left(\frac{\sigma}{r}\right) \tag{8}$$

where σ is the surface tension. Eqs.(1)–(5) and Eq. (8) form a set of six equations, including five coupled differential equations. The resulting set of first order, non linear, coupled ordinary differential equations is solved numerically with a fourth order Runge–Kutta method using the following boundary conditions:

$$u_\mathrm{l}|_{x=L_\mathrm{g}} = u_\mathrm{v}|_{x=L_\mathrm{g}} = 0, \quad P_\mathrm{v}|_{x=L_\mathrm{g}} = P_\mathrm{sat}$$
$$r|_{x=L_\mathrm{g}} = r_\mathrm{max}, \quad P_\mathrm{l}|_{x=L_\mathrm{g}} = P_\mathrm{sat} - \frac{\sigma}{r_\mathrm{max}} \tag{9}$$

where L_g is the length of the groove and P_sat is the saturation pressure. The value of r_max depends on the heat transfer rate. It is assumed that the constant value of the meniscus curvature radius, r_0 measured all along the grooves when the TPHS does not work, remains constant in the middle of the adiabatic area in operating conditions. Indeed, as in the adiabatic area no phase change occurs, we assume that in a cross-section, the ratio between liquid and vapour remains constant and thus the meniscus radius does not vary. This is not the case in the evaporator and condenser zones where it increases or decreases due to evaporation or condensation. The value of r_max is obtained when the meniscus curvature radius is equal to r_0 in the adiabatic area through a shooting method.

The hydrodynamic model allows the calculation of the maximum heat transfer capability q_max. The value of q_max is obtained when the meniscus curvature radius reaches a minimum value r_min [22]:

$$r_\mathrm{min} = \frac{l_\mathrm{g}}{2\cos\theta} \tag{10}$$

where l_g is the groove width and θ the contact angle between the meniscus and the wall.

4. Experimental results

The TPHS has been tested in horizontal and in vertical orientations. For this last position, the gravity field allows the liquid to come back from the condenser to the evaporator (thermosyphon orientation). The TPHS has not been tested in vertical unfavourable position, the condenser being above the evaporator, because the capillary pressure is too small to overcome the gravity forces on a height equal to 230 mm.

For PEMFC cooling, the TPHS will be vertical inside the PEMFC with the heat sink located on the top of the fuel cell. In this configuration, the liquid flow is gravity-assisted and the grooves are used to distribute the liquid on the whole evaporator area. The TPHS filling corresponds to a liquid height at the bottom equal to 2 cm in vertical orientation (measured at 20 °C). The liquid flow rate in the heat sink is equal to $35\,\mathrm{l\,h^{-1}}$ during the experiment.

Figs. 5–7 show experimental results obtained in vertical orientation. Fig. 5 shows the temperature difference between the wall temperature T_w and the wall temperature at the end of the condenser $T_\mathrm{w\,min}$ versus the non dimen-

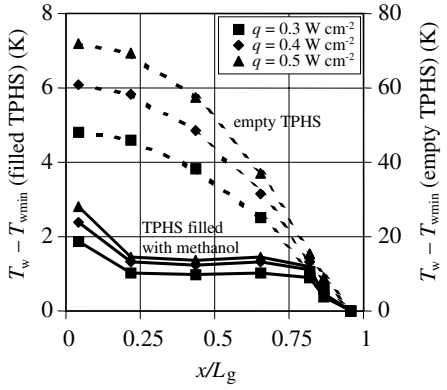

Fig. 5. Wall temperature profile along the empty TPHS and the TPHS filled with methanol ($T_{sat} = 70$ °C).

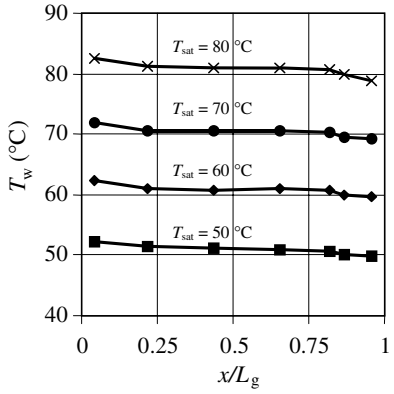

Fig. 6. Wall temperature profile along the TPHS filled with methanol for different saturation temperatures ($q = 0.5$ W cm^{-2}).

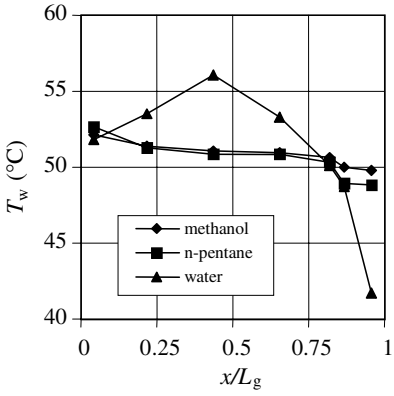

Fig. 7. Wall temperature profile along the TPHS filled with methanol, *n*-pentane and water ($q = 0.5$ W cm^{-2}).

sional coordinate x/L_g ($x = 0$ at the extremity of the evaporator and $x = L_g$ at the end of the condenser). The experimental results are shown for three imposed heat fluxes at the evaporator: $q = 0.3$ W cm^{-2}, $q = 0.4$ W cm^{-2} and $q = 0.5$ W cm^{-2} at a working temperature equal to 70 °C. The solid lines correspond to the TPHS filled with methanol and the dashed lines correspond to the empty TPHS. For heat fluxes varying from 0.3 W cm^{-2} to 0.5 W cm^{-2}, the maximum temperature difference between the condenser and the evaporator varies from 1.9 K to 2.8 K for the filled TPHS. The temperature profile is very homogeneous on the whole evaporator area, except in the pool between $x = 0$ cm and $x = 2$ cm, where convective heat transfer occurs in the liquid rather than vaporization at the liquid–vapour interface. Thus, the heat transfer coefficient is lower in the pool than in the upper side of the evaporator, which conducts to higher temperature gradients for a same imposed heat flux. The maximum temperature difference along the evaporator varies from 1 K to 1.6 K for heat fluxes varying from 0.3 W cm^{-2} to 0.5 W cm^{-2}. For the empty TPHS, the maximum temperature difference between the condenser and the evaporator reaches 47.9 K, 61.0 K and 72.1 K for $q = 0.3$ W cm^{-2}, $q = 0.4$ W cm^{-2} and $q = 0.5$ W cm^{-2}, respectively. It is 20 times higher than in two-phase flow working configuration.

The temperature profile along the TPHS is shown in Fig. 6 for different working temperatures varying from 50 °C to 80 °C. The working temperature does not have a significant influence on the longitudinal temperature profile. The temperature gradients are higher in the condenser than in the evaporator, which is mainly due to a condenser area lower than the evaporator area for the same heat transfer rate.

Fig. 7 shows the wall temperature profile for a working temperature equal to 50 °C and three different working fluids that are chemically compatible with copper: methanol, *n*-pentane and water. The maximum temperature difference between the evaporator and the condenser is small for methanol and *n*-pentane for which the wettability on the copper is high. As a result, the wall is well wetted and the vaporization is high. On the contrary, water does not wet copper. Dropwise condensation occurs on the condenser fins between the grooves, but the drops do not enter in the grooves, and thus the liquid is not drained by them. The liquid flows only on the groove fins and at the middle of the evaporator the temperature is less homogeneous than that obtained for methanol and *n*-pentane. The maximum temperature is located in the middle of the evaporator, which shows that one part of the heat is transferred by heat conduction through the wall from the evaporator centre to the pool or to the condenser.

The maximum temperature difference between the condenser and the evaporator is lower than 3.5 K for methanol and it reaches 9.5 K for *n*-pentane. The results are less satisfactory with *n*-pentane because the condensation heat transfer is lower than the one obtained with methanol. Indeed, let us consider the Nusselt expression for the calculation of the average condensation heat transfer h_{cond} on a vertical plate in laminar conditions:

$$h_{cond} = 0.943\left[\frac{\rho_l g(\rho_l - \rho_v)\lambda_l^3 h_{lv}}{\mu_l(T_{sat} - T_w)L_{cond}}\right]^{1/4}$$

with ρ_l and ρ_v the liquid and vapour densities, λ_l and μ_l the liquid thermal conductivity and the dynamic viscosity, h_{lv}

the latent heat of vaporization, T_{sat} the saturation temperature and T_w the wall temperature. L_{cond} is the condenser length. For a saturation temperature equal to 60 °C, the heat transfer coefficient for *n*-pentane is 2.2 times smaller than the one of methanol, because of its low latent heat of vaporisation and its low thermal conductivity.

Thermal tests in horizontal orientation were conducted to determine the behaviour of the two-phase heat spreader, when the liquid motion is due to capillary forces rather than to volume forces. A special care has been focused on the horizontal orientation of the TPHS, because gravity is a non negligible parameter of the TPHS performances. Fig. 8 shows the wall temperature profile for a saturation temperature equal to 70 °C and heat fluxes varying from 0.1 to 1.1 W cm^{-2}. The working fluid is methanol. The temperature profile is similar to the one obtained in thermosyphon orientation for heat fluxes lower than 0.9 W cm^{-2}, but it is more homogeneous at the evaporator extremity, which is not filled with liquid in this working configuration. The maximum temperature difference along the evaporator is equal to 0.9 K and 1.3 K for heat fluxes equal to 0.3 W cm^{-2} and 0.5 W cm^{-2}, respectively. For heat fluxes higher than 0.9 W cm^{-2}, the TPHS reaches its capillary limit at the end of the evaporator: the pressure drops in the liquid and in the vapour are too high to allow the liquid to be drained all along the evaporator.

Fig. 9 shows the comparison between the measured and the calculated meniscus curvature radii along the TPHS in horizontal orientation. The experimental results for heat fluxes equal to 0.5 W cm^{-2}, 0.7 W cm^{-2} and 0.9 W cm^{-2} at different x locations are symbolised by stars, triangles and diamonds, respectively. Dashed, solid and point dashed lines correspond to calculated radii for each heat flux, respectively. The meniscus radius is equal to 850 μm all along the grooves when the TPHS does not work.

The measurements obtained by confocal microscopy are averaged over ten grooves located at a same x position to calculate the meniscus curvature radius. The average standard deviation of these measurements is about 50 μm. A measurement example across five grooves is shown in

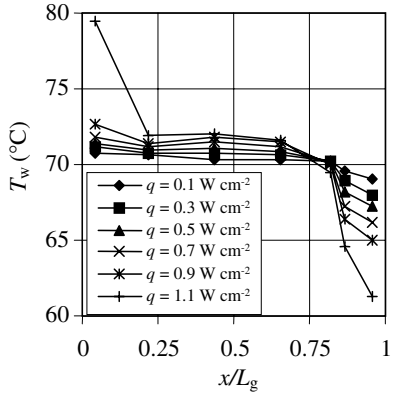

Fig. 8. Wall temperature profile along the TPHS in horizontal orientation.

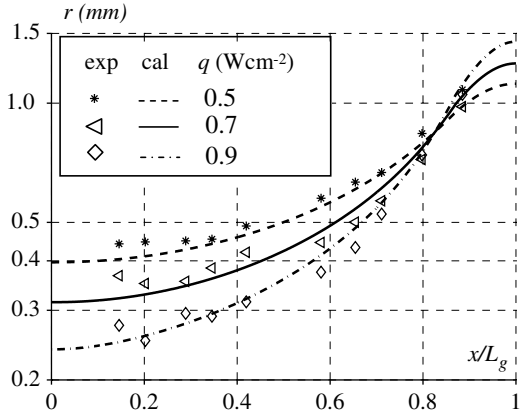

Fig. 9. Measured and calculated meniscus curvature radii along the TPHS in horizontal orientation ($T_{sat} = 71$ °C).

Fig. 10 in the condenser area ($x/L_g = 0.88$) for a heat flux equal to 0.7 W cm^{-2}. On the fin top the surface profile is dispersed because of the surface roughness on the copper wall. In the evaporator area, as the meniscus radius is small, only the middle part of the meniscus can be measured. Indeed the slope of the meniscus at the junction with the grooves is higher than the maximum measuring angle of the optical sensor, which is equal to 27° for specular reflection. Thus, the identified meniscus radii are less precise in the evaporator region than in the condenser region. Nevertheless, the meniscus curvature observations show that even in the evaporator section, the meniscus is always hanged on the top of the grooves for the observed zones. The extremities of the TPHS cannot be observed, because the TPHS closing system prevents the optical sensor positioning near these extremities. Thus, the grooves can only be observed from $x = 25$ mm to $x = 205$ mm.

The experimental results fit well the calculated meniscus radii that are obtained with a value of the interfacial shear stress equal to zero. The interfacial shear stress has generally a non negligible influence on two-phase device perfor-

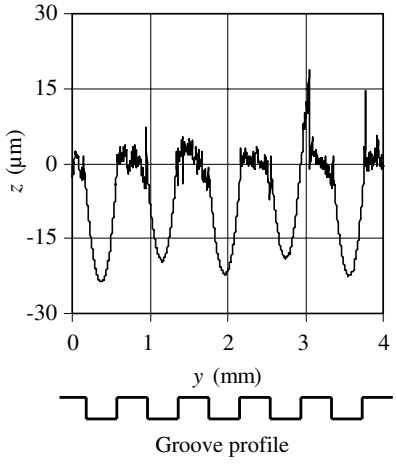

Fig. 10. Meniscus curvature radii measured inside the grooves by confocal microscopy ($T_{sat} = 71$ °C).

mances such as micro heat pipes, because the vapour cross-section is small compared to the liquid cross-section. In this TPHS, the vapour cross-section is ten times higher than the liquid cross-section, which reduces the influence of τ_{int}. Furthermore, the interfacial shear stress due to the counter-current vapour flow is reduced because evaporation occurs all along the grooves.

Fig. 11 shows the calculated liquid and vapour pressures for $q = 0.5\ \mathrm{W\,cm^{-2}}$ and $T_{sat} = 71\ ^\circ\mathrm{C}$. The vapour and the liquid pressure drops are equal to 3 Pa and 26 Pa, respectively. Fig. 12 shows the corresponding liquid and vapour velocities for the same conditions. The decrease and increase of the velocities correspond to the heat source and heat sink sections.

It has been shown experimentally that the maximum heat transfer capability of the TPHS, q_{max} is equal to $0.9\ \mathrm{W\,cm^{-2}}$ for a saturation temperature of 71 °C (Fig. 8). For q_{max}, the value of the minimum meniscus radius r_{min} at the end of the evaporator is equal to 240 μm (Fig. 9). The corresponding contact angle is equal to 33°. This value of r_{min} is used to calculate the maximum heat transfer capability of the TPHS versus the saturation temperature as shown in Fig. 13. The maximum heat transfer capability increases with the saturation temperature, which is due to the decrease of the liquid viscosity at high temperature.

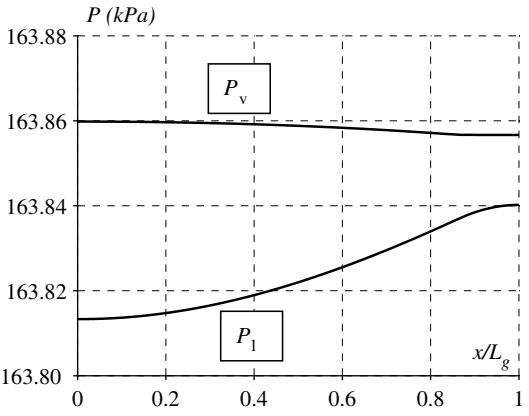

Fig. 11. Liquid and vapour pressures for $q = 0.5\ \mathrm{W\,cm^{-2}}$ and $T_{sat} = 71\ ^\circ\mathrm{C}$.

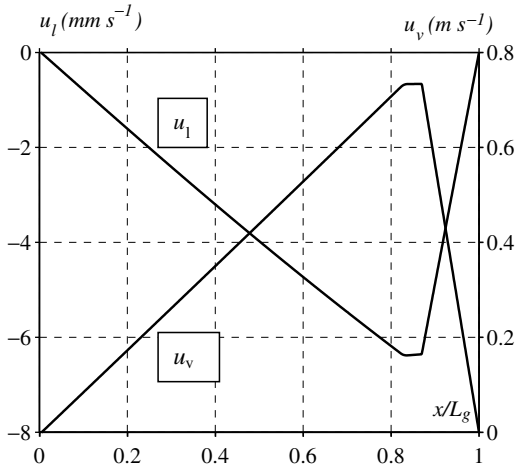

Fig. 12. Liquid and vapour velocities for $q = 0.5\ \mathrm{W\,cm^{-2}}$ and $T_{sat} = 71\ ^\circ\mathrm{C}$.

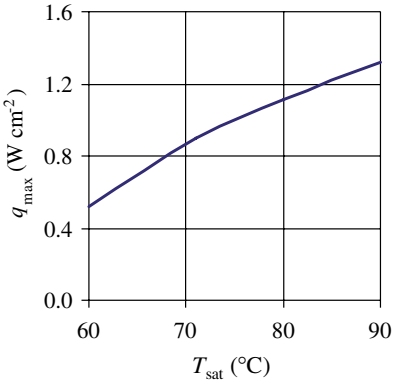

Fig. 13. Calculated maximum heat transfer capability versus T_{sat}.

5. Conclusion

A two-phase heat spreader with rectangular microgrooves has been tested in horizontal and favourable vertical orientations. The evaporator area is high compared to the condenser area, which corresponds to heat dissipation inside a PEMFC. The results obtained with the TPHS filled with methanol show a temperature difference between the evaporator and the condenser lower than 3 K for working conditions similar to those of a PEMFC (evaporator heat flux equal to $0.5\ \mathrm{W\,cm^{-2}}$ and working temperature equal to 70 °C). The temperature variation is lower than 1.6 K all along the evaporator. The results show that the choice of the working fluid is important to obtain good thermal performances either in vertical thermosyphon orientation or in horizontal orientation.

In horizontal orientation, a confocal microscope has been used to measure the meniscus curvature radius along a groove. A good agreement has been found between the experimental and theoretical results obtained with a two-phase flow model, based on the balance equations and the Young–Laplace law. These first measurements obtained by confocal microscopy are very promising for a better understanding of the TPHS working mechanisms.

Acknowledgement

This project was supported by the French Ministry of Education and Research and the CNRS. We are indebted to the French laboratories LAAS, LE, LET and LEMTA for their collaboration.

References

[1] M. Lallemand, F. Lefèvre, Micro/mini heat pipes for the cooling of electronic devices, in: 13th International Heat Pipe Conference, Shanghaï, China, 2004, pp. 12–22.

[2] F. Lefèvre, M. Lallemand, Coupled thermal and hydrodynamic models of flat micro heat pipes for the cooling of multiple electronic components, Int. J. Heat Mass Transfer 49 (2006) 1375–1383.

[3] B. Badran, F.M. Gerner, P. Ramada, T. Henderson, K.W. Baker, Experimental results for low-temperature silicon micromachined micro heat pipe arrays using water and methanol as working fluids, Exp. Heat Transfer 10 (1997) 253–272.

[4] S.W. Kang, D. Huang, Fabrication of star grooves and rhombus grooves micro heat pipe, J. Micromech. Microeng. 12 (2002) 525–531.

[5] M. Le Berre, S. Launay, V. Sartre, M. Lallemand, Fabrication and experimental investigation of silicon heat pipes for cooling electronics, J. Micromech. Microeng. 13 (2003) 436–441.

[6] S.H. Moon, G. Hwang, S.C. Ko, Y.T. Kim, Experimental study on the thermal performance of micro-heat pipe with cross-section of polygon, Microelectron. Reliab. 44 (2004) 315–321.

[7] Y.X. Wang, G.P. Peterson, Analysis of wire-bonded micro heat pipe arrays, J. Thermophys. Heat Transfer 16 (3) (2002) 346–355.

[8] Y. Avenas, B. Mallet, C. Gillot, A. Bricard, C. Schaeffer, G. Poupon, E. Fournier, Thermal spreaders for high heat flux power devices, in: 7th Therminic Workshop, Paris, France, 2001, pp. 59–63.

[9] Y. Cao, M. Gao, Experiments and analyses of flat miniature heat pipes, J. Thermophys. Heat Transfer 11 (2) (1997) 158–164.

[10] R. Hopkins, A. Faghri, D. Khrustalev, Flat miniature heat pipes with micro capillary grooves, J. Heat Transfer 121 (1999) 102–109.

[11] C. Perret, Y. Avenas, C. Gillot, J. Boussey, C. Schaeffer, Integrated cooling devices in silicon technology, Eur. Phys. J. AP 18 (2002) 115–123.

[12] L. Zhang, T. Ma, Z. Zhang, X. Ge, Experimental investigation on thermal performance of flat miniature heat pipes with axial grooves, in: 13th International Heat Pipe Conference, Shanghaï, China, 2004, pp. 206–211.

[13] S. Kandhekar, M. Groll, V. Luckchoura, W. Findl, J. Zhuang, Micro heat pipes for stacked 3D microelectronic modules, in: International Electronic Packaging Technical Conference and Exhibition, Maui, Hawaii, 2003, p. 7.

[14] Y. Avenas, M. Ivanova, C. Schaeffer, R. Perret, J.L. Sanchez, Etude et réalisation de caloducs à réseau capillaire à picots carrés pour le refroidissement en électronique, Congrès SFT 2003, Grenoble, France, 2003, pp. 913–918.

[15] B. Gromoll, Micro cooling systems for high density packaging, Rev. Gén. Therm. 37 (1998) 781–787.

[16] D.S. Shen, R.T. Mitchell, D. Dobranich, D.R. Adkins, M.R. Tuck, Micro heat spreader enhanced heat transfer in MCMs, in: IEEE Multi-Chip-Module Conference, Santa Cruz, USA, 1995, pp. 189–194.

[17] S.W. Kang, S.H. Tsai, H.C. Chen, Fabrication and test of radial grooved micro heat pipes, Appl. Therm. Eng. 22 (2002) 1559–1568.

[18] S.W. Kang, S.H. Tsai, M.H. Ko, Metallic micro heat pipe heat spreader fabrication, Appl. Therm. Eng. 24 (2004) 299–309.

[19] Y. Wang, K. Vafai, An experimental investigation of the thermal performance of an asymmetrical flat plate heat pipe, Int. J. Heat Mass Transfer 43 (2000) 2657–2668.

[20] L. Lin, R. Ponnappan, J. Leland, High performance miniature heat pipe, Int. J. Heat Mass Transfer 45 (2002) 3131–3142.

[21] J. Min, R.L. Webb, Condensate formation and drainage on typical fin materials, Exp. Therm. Fluid Sci. 25 (2001) 101–111.

[22] A. Faghri, Heat pipe science and technology, Taylor and Francis, London, 1995.